

MIT Open Access Articles

Impact of microstructure on the electron-hole interaction in lead halide perovskites

The MIT Faculty has made this article openly available. **Please share** how this access benefits you. Your story matters.

Citation: Soufiani, Arman Mahboubi et al. "Impact of microstructure on the electron-hole interaction in lead halide perovskites." *Energy & Environmental Science* 10, 6 (May 2017) : 1358-1366. ©2017 The Royal Society of Chemistry

As Published: <http://dx.doi.org/10.1039/c7ee00685c>

Publisher: Royal Society of Chemistry (RSC)

Persistent URL: <https://hdl.handle.net/1721.1/124562>

Version: Author's final manuscript: final author's manuscript post peer review, without publisher's formatting or copy editing

Terms of use: Creative Commons Attribution-Noncommercial-Share Alike





Cite this: DOI: 10.1039/c7ee00685c

Received 11th March 2017,
Accepted 15th May 2017

DOI: 10.1039/c7ee00685c

rsc.li/ees

Impact of microstructure on the electron–hole interaction in lead halide perovskites†

Arman Mahboubi Soufiani,^{‡a} Zhuo Yang,^{‡b} Trevor Young,^a Atsuhiko Miyata,^b Alessandro Surrente,^b Alexander Pascoe,^c Krzysztof Galkowski,^{bd} Mojtaba Abdi-Jalebi,^e Roberto Brenes,^f Joanna Urban,^b Nan Zhang,^b Vladimir Bulović,^e Oliver Portugall,^b Yi-Bing Cheng,^{id c} Robin J. Nicholas,^g Anita Ho-Baillie,^{id *a} Martin A. Green,^{id a} Paulina Plochocka^{*b} and Samuel D. Stranks^{id *ef}

Despite the remarkable progress in the performance of devices based on the lead halide perovskite semiconductor family, there is still a lack of consensus on their fundamental photophysical properties. Here, using magneto-optical transmission spectroscopy we elucidate the impact of the microstructure on the Coulomb interaction between photo-created electron–hole pairs in methylammonium lead triiodide (MAPbI₃) and the triple-cation lead mixed-halide composition, Cs_{0.05}(MA_{0.17}FA_{0.83})_{0.95}Pb(I_{0.83}Br_{0.17})₃ (Cs: cesium, MA: methylammonium, FA: formamidinium) by investigating thin films with a wide range of grain sizes from tens of nanometers to microns. At low temperatures, in which thermal fluctuations of the interactions are frozen and the rotational disorder of the organic cation is negligible, the exciton binding energy and reduced effective mass of carriers remain effectively unchanged with grain size. We conclude that the microstructure plays a negligible role in the Coulomb interaction of the photo-created electron–hole pairs, in contrast to previous reports. This renewed understanding of the relationship between these fundamental electronic properties and the microstructure is critical for future fundamental studies and improving device design.

Introduction

Solar cells based on lead halide perovskites (with general chemical formula of ABX₃; A = CH₃NH₃⁺ [methylammonium, MA], HC(NH₂)₂⁺ [formamidinium, FA] or Cs⁺; B = Pb²⁺; X = I⁻,

Broader context

Metal halide perovskites such as methylammonium lead iodide (MAPbI₃) and alloyed mixed-cation lead mixed-halide counterparts such as Cs_{0.05}(MA_{0.17}FA_{0.83})_{0.95}Pb(I_{0.83}Br_{0.17})₃ are creating enormous excitement for their use in high-performance solar cells with potential for exceptionally low capital-intensity for production. An important parameter that dictates the design of a solar cell is the strength of the Coulomb interaction between the photo-generated electron in the conduction band and the hole in the valence band (*i.e.* the exciton binding energy). Recently, it has been suggested that the exciton binding energy of the perovskite material is influenced by the size of the grains of the perovskite film, and therefore different device design will be required depending on the grain size. Here, we perform magneto-optic measurements on films with different grain sizes to directly show that the microstructure has a negligible influence on the excitonic properties in the samples, and that excitons do not play a significant role in films with any of the polycrystalline morphologies studied. This means that excitons should not be a factor for the design of optoelectronic devices based on polycrystalline MAPbI₃ and similar materials with different grain sizes, making future device architecture optimisation less constrained.

Br⁻ or Cl⁻) have achieved astonishingly high power conversion efficiencies exceeding 22% in only seven years since they were first used as sensitizers in photovoltaic solar cells.^{1–3} Since then, the remarkable properties of these crystalline semiconductors, such as the tunability of their optoelectronic properties through fabrication of layers with different morphologies, compositions

^a Australian Centre for Advanced Photovoltaics, School of Photovoltaic and Renewable Energy Engineering, University of New South Wales, Sydney, NSW 2052, Australia. E-mail: a.ho-baillie@unsw.edu.au

^b Laboratoire National des Champs Magnétiques Intenses, CNRS-UGA-UPS-INSA, 143 Avenue de Rangueil, 31400 Toulouse, France. E-mail: paulina.plochocka@lncmi.cnrs.fr

^c Department of Materials Science and Engineering, Monash University, Clayton, Vic 3800, Australia

^d Institute of Experimental Physics, University of Warsaw, Pasteura 5, 02-093 Warsaw, Poland

^e Cavendish Laboratory, University of Cambridge, J. J. Thomson Avenue, Cambridge CB3 0HE, UK. E-mail: sds65@cam.ac.uk

^f Research Laboratory of Electronics, Massachusetts Institute of Technology, Cambridge, MA 02139, USA

^g Clarendon Laboratory, University of Oxford, Parks Road, Oxford OX1 3PU, UK

† Electronic supplementary information (ESI) available. See DOI: 10.1039/c7ee00685c

‡ These authors contributed equally to this work.

and crystal qualities,^{4–7} have been further exploited to develop a variety of promising optoelectronic devices.^{8–11}

As for any emerging semiconductor material deployable in optoelectronic devices, the strength of the Coulomb interaction between the photo-generated electron in the conduction band and the hole in the valence band is of high importance. This was a focus of several studies on perovskites about two decades ago^{12–14} and has recently regained attention^{15–18} mainly due to the promising outlook of perovskites for solar photovoltaics,¹⁰ light-emitting diodes¹¹ and lasing applications¹⁹ with polycrystalline thin films and single crystals having superior quality to those synthesized two decades ago.

The latest studies have come to a consensus that the exciton binding energy – alternatively known as effective Rydberg energy (Ry^*) in the Wannier–Mott exciton model – of well-studied $MAPbI_3$ and $MAPbBr_3$ polycrystalline thin films is ~ 5 – 12 meV^{15,17,18} and ~ 25 meV^{16,18} in the room temperature phase, respectively. These low values, with respect to thermal energy at room temperature ($k_b \times T \approx 26$ meV; k_b is the Boltzmann constant and T is the temperature in Kelvin), are due to generally weak many-body effects (*i.e.* Coulombic interactions) in these semiconductor systems.²⁰ Nevertheless, there is ongoing debate concerning the possible tunability of this parameter, and there is speculation that variations of the microstructure and hence crystal quality of the perovskite layer^{21,22} influence the photo-excited exciton binding energies.

It has been proposed that disordered organic cation dipole domains in small and defective crystals with a large portion of poly-crystallinity can create a large electrostatic potential fluctuation which causes a substantial screening of the photo-generated excitons.²² This could lead to a very small value of Ry^* on the order of ~ 2 – 5 meV^{23,24} meaning that the material behaves as if in the non-excitonic regime. On the other hand, large and defect-free crystals can exhibit an order of magnitude greater values of Ry^* .^{22,25} As a result, one current hypothesis is that it is not possible to assign a universal value to the exciton binding energy of the commonly used hybrid lead halide perovskites.

A key consequence of this hypothesis could be a change in the working regime (*i.e.* photo-excited carrier dissociation and transport) of solar cells fabricated from active layers with diverse microstructures. Knowledge of the value of the exciton binding energy is essential because it determines the nature of the majority of the photo-generated species (*i.e.* free carriers *versus* excitons) in a semiconductor. For devices comprised of materials with binding energies greater than the probability of thermal dissociation at the working temperature, there would need to be an additional mechanism for exciton dissociation into free carriers, such as an additional heterojunction, through which they can readily contribute to the photocurrent.²⁶ In the case that the binding energies are so low that the fraction of photo-excited species that are excitons is negligible, the n- and p-type contacts in the heterojunction structure of the solar cell (*cf.* most perovskite solar cells) would simply act as charge-selective contacts for the photo-generated electrons and holes, respectively, facilitating simpler device designs. Altogether, these

points highlight the need to fully understand the exciton–morphology relationship.

Here, we elucidate the influence of the microstructure, manipulated through the perovskite fabrication method, on the exciton binding energy Ry^* and the excitonic reduced mass (μ) for a variety of $MAPbI_3$ crystal sizes covering the size range reported in devices to date. The impact of the local order and the degree of poly-crystallinity on electron–hole interaction is unraveled through a direct measurement of Ry^* and μ for thin films with different grain sizes. These measurements are performed at low temperature (2 K) at which the impact of MA^+ thermal orientational dynamic rearrangement is mitigated. We provide strong evidence that the grain size has negligible influence on the exciton binding energy and effective mass in $MAPbI_3$ and, thus, does not affect the dissociation probability of the bulk excitons and their stability in the photo-excited charge carrier population.

Results and discussion

Sample morphology

A wide range of fabrication methods, from single-step²⁷ to sequential deposition²⁸ and solution-processed²⁹ to vapor-assisted³⁰ techniques, have been employed to fabricate the active layer of perovskite optoelectronic devices in the literature. Here, different deposition methods, which have been shown to give corresponding high-performance solar cells with power conversion efficiencies of $>16\%$,^{6,31,32} are used to controllably tune the perovskite grain size in the films. These samples with $MAPbI_3$ chemical composition but fabricated *via* different methods with various resulting morphologies simulate the range of different degrees of structural disorder and poly-crystallinity in the $MAPbI_3$ layer in high-performance perovskite devices fabricated to date.²² The top-view scanning electron microscope (SEM) images of the samples are presented in Fig. 1A–D. The morphologies vary from a planar polycrystalline film with grain sizes of 772 ± 227 nm³² (A; large grain polycrystalline annotated LPC) and polycrystalline film with grain sizes of 214 ± 57 nm³¹ (B; small grain polycrystalline annotated SPC), to small crystals of 291 ± 64 nm fabricated by a two-step dipping technique⁶ (C; annotated SC) and also perovskite infiltrated into a ~ 2 μ m thick mesoporous aluminum oxide scaffold (mp- Al_2O_3) with grain sizes of <50 nm (D; annotated MP). As can be seen in the top-view SEM image of the MP sample, there is no visible capping layer formed on top of the mesoscopic phase and, therefore, a potential artefact from the larger grain sizes of a capping layer does not influence the related data analysis.

Magneto-optical transmission measurements

Studying the optical behavior of excitons under external fields has proven to be a powerful tool to reveal properties of these quasi-particles in semiconductors.³³ Here, we conducted optical transmission measurements under high magnetic fields (B) up to 150 T on the samples presented in Fig. 1. Typical transmission

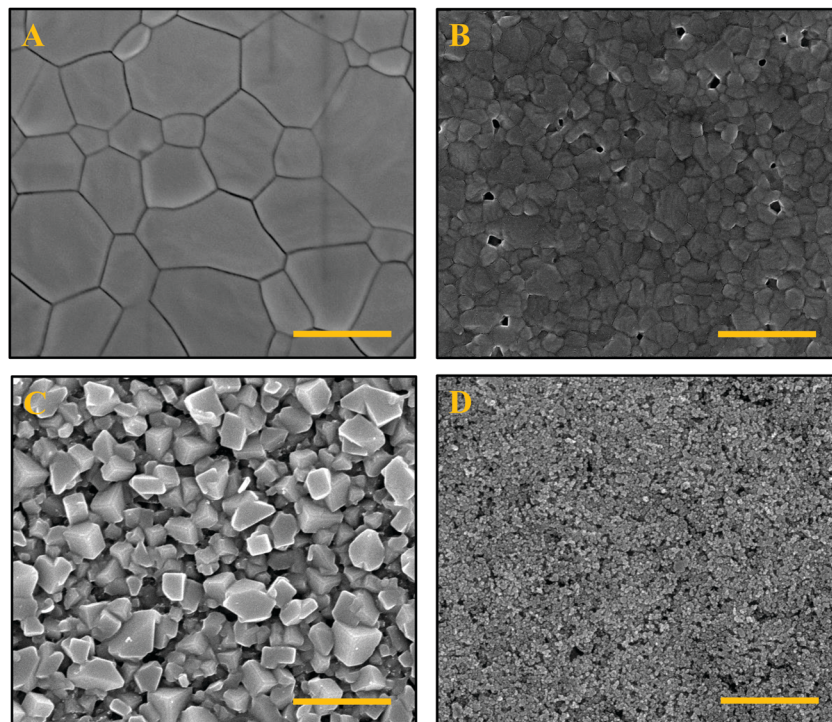


Fig. 1 Morphology of MAPbI₃ samples. Top-view SEM images of MAPbI₃ layer with various morphologies fabricated on glass substrates. (A) Polycrystalline thin film with grain sizes 772 ± 227 nm (LPC). (B) Polycrystalline thin film with grain sizes 214 ± 57 nm (SPC). (C) Small crystals of MAPbI₃ fabricated by the two-step solution-processed dipping technique, with resulting crystal sizes 291 ± 64 nm (SC). (D) MAPbI₃ infiltrated into a thick mesoporous-Al₂O₃ scaffold with grain sizes <50 nm (MP). Scale bars are 1 μm.

spectra for the large grain polycrystalline thin film sample, showing a strong 1s excitonic transition, are given in Fig. 2A. For unambiguous identification of the weaker optical transitions, we show in Fig. 2B the ratio of the transmission spectrum at a specific high magnetic field over the transmission spectrum taken at zero field, illustrating the free-carrier transitions. In Fig. 2C we show transmission measurements at several monochromatic probe energies under very high magnetic field (<150 T) achieved using a short pulse technique. The related spectra for other morphologies are provided in the ESI,† Fig. S1–S3.

We note that a hydrogen-like excitonic behavior³⁴ can be assumed for MAPbI₃ in the low-temperature orthorhombic phase. The strong minimum in the transmission spectra (Fig. 2A), attributed to the 1s state of the hydrogen-like free exciton,¹⁷ blue shifts with increase of the magnetic field. The second minimum, located at slightly higher energies than the 1s state, is attributed to the first excitonic excited state (labelled as 2s in Fig. 2A) and also exhibits a blue-shift with magnetic field.

The Landau levels, the free carrier states with quantum numbers $N = 0, 1, 2, \dots$ formed by quantization of the particle's motion in the plane perpendicular to the magnetic field,³³ can be observed at higher energies in the strong magnetic field regime in which $\hbar\omega_c \gg Ry^*$ ($\hbar\omega_c = \hbar eB/\mu$), where \hbar and e are Planck's constant and the electron charge, respectively, ω_c is the cyclotron frequency, and $\mu^{-1} = m_e^{-1} + m_h^{-1}$ is the reduced mass of the exciton (m_e and m_h are electron and hole effective masses, respectively). The free carrier Landau level transitions are dominant at high magnetic fields with transition energy

described by $E(B) = E_g + (N + 1/2)\hbar\omega_c$ ^{16,17} where E_g is the bandgap. We can then fit the measured optical transitions between Landau levels to extract the reduced mass, μ , independently of the exciton binding energy. The value of the reduced mass thus obtained is used as a fixed parameter in the fit of the hydrogen-like excitonic transitions to extract the exciton binding energy, based on a model which describes the hydrogen atoms in high magnetic field.³⁵ In this model, a dimensionless parameter γ , defined as $\gamma = \hbar\omega_c/2Ry^*$, is used. Makado and McGill calculated the transition energies of excitonic states $E_n(\gamma)$ as a function of quantum number n up to 4 and γ ranging from 0 to 10.³⁵ Given values of the magnetic field B and the reduced mass μ , the binding energy Ry^* is the only fitting parameter to fit the energies of the full set of hydrogenic transitions.

The complete set of these excitonic and free carrier transition energies for the LPC sample is plotted in the fan diagram in Fig. 2D. The observation of many Landau levels in the magnetic field <150 T allows precise determination of the reduced mass. Knowledge of the reduced mass in turn imposes strong constraints on fitting the excitonic binding energy. An additional influential constraint on the value of the binding energy is set if the higher excitonic transition resonances such as the 2s state are resolved, as for the LPC morphology. The observation of a well-resolved 2s state at intermediate magnetic field fixes the transition energy of 2s at zero magnetic field using the model described earlier. The energy separation of 1s–2s at zero magnetic field follows the series of 3D hydrogen-like energy states, $E_n = E_g - Ry^*/n^2$ where E_n is the excitonic transition

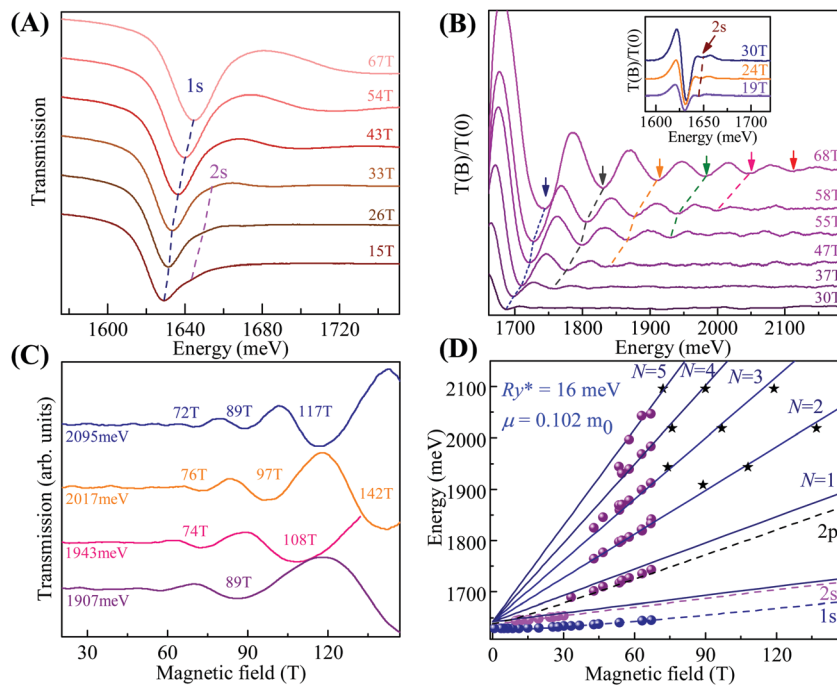


Fig. 2 Magneto-optical transmission spectrum and fan chart measured at 2 K. (A) Sequence of typical optical transmission spectra of the LPC sample measured at the indicated magnetic fields which show the 1s and 2s excitonic transitions with increased transmission. (B) Sequences of the ratios of the transmission spectra in magnetic field $T(B)$ to that measured at zero field $T(0)$. The resonant absorption features of the free carrier Landau levels correspond to minima. (C) Typical results of the low temperature monochromatic transmission as a function of magnetic field obtained by the short pulse technique. (D) Fan chart of MAPbI_3 for the large grain polycrystalline sample. The circular data points are from long pulse field measurements and the star symbol points are collected by short pulse mega-gauss measurements. The solid lines and the dashed lines are the fits to the set of Landau levels and the excitonic transitions, respectively.

energy at zero magnetic field. This gives a strong constraint on the exciton binding energy.

The fitting to the hydrogen-like excitonic (dashed lines) and free carrier (solid lines) transitions, as explained in further detail in ref. 16, 17 and 35, is presented in Fig. 2D and the Ry^* and μ values for the LPC sample are calculated to be 16 ± 1 meV and $0.102 \pm 0.002m_0$, respectively. For the morphologies other than LPC (*i.e.* SPC, SC and MP), the identification of free carrier transitions at high energies allows us to obtain the values of the reduced masses. The extracted μ values are presented in Table 1 and are very close to the value originally reported by Miyata *et al.* ($\mu = 0.104 \pm 0.003m_0$).¹⁷ Importantly, we find that the microstructure has negligible influence on the reduced mass. This indicates that the polaron coupling constant, incorporating the effective longitudinal optical (LO) phonon energy and the optical and static dielectric constants of the medium, which couples to the band-edge bare effective masses to form the polaronic masses,^{18,36} is only minimally influenced by the variation in microstructure.

In the absence of a clear observation of the 2s excitonic transitions for the SPC, SC and MP samples, the global fit to the full excitonic and free-carrier transitions was employed and the resulting unchanged Ry^* values are presented in Table 1. To visualize the negligible change in the optical response under external magnetic fields of the MAPbI_3 films with different morphology, the overlaid fan diagrams of the complete set of excitonic and free carrier optical transitions after shifting by

Table 1 Summary of the parameters of the fits to the full Landau fan chart for the four different morphologies of MAPbI_3 in the low temperature (2 K), orthorhombic phases. The figures in the brackets are the error estimates of the parameters

	Size distribution (nm)	E_g (meV)	μ (m_0)	Ry^* (meV)
Large polycrystalline	772(227)	1642(2)	0.102(0.002)	16(1)
Small polycrystalline	214(57)	1643(2)	0.105(0.002)	16(4)
Small crystal	291(64)	1639(2)	0.109(0.002)	16(4)
Mesoporous	< 50	1638(2)	0.107(0.003)	16(4)

the corresponding bandgap offsets are presented in Fig. 3A. Here we clearly show that these MAPbI_3 samples, although composed of dramatically different grain sizes and morphologies, exhibit similar magneto-optical behaviour. Furthermore, the XRD patterns (Fig. S4, ESI[†]) show that the MAPbI_3 SPC and SC thin films have some PbI_2 impurities, indicating that the presence of small amounts of PbI_2 also does not affect the excitonic properties of perovskites. We also note that, although the changes in the grain size and morphology do not influence the low-temperature excitonic properties of perovskites, they can affect the optoelectronic response of these materials including their PL behaviour and the fraction of retained tetragonal phase within the orthorhombic phase upon lowering the temperature.^{37–39}

It was recently shown that when replacing MA^+ by a larger monovalent organic cation, formamidinium ($\text{HC}(\text{NH}_2)_2^+$, FA),

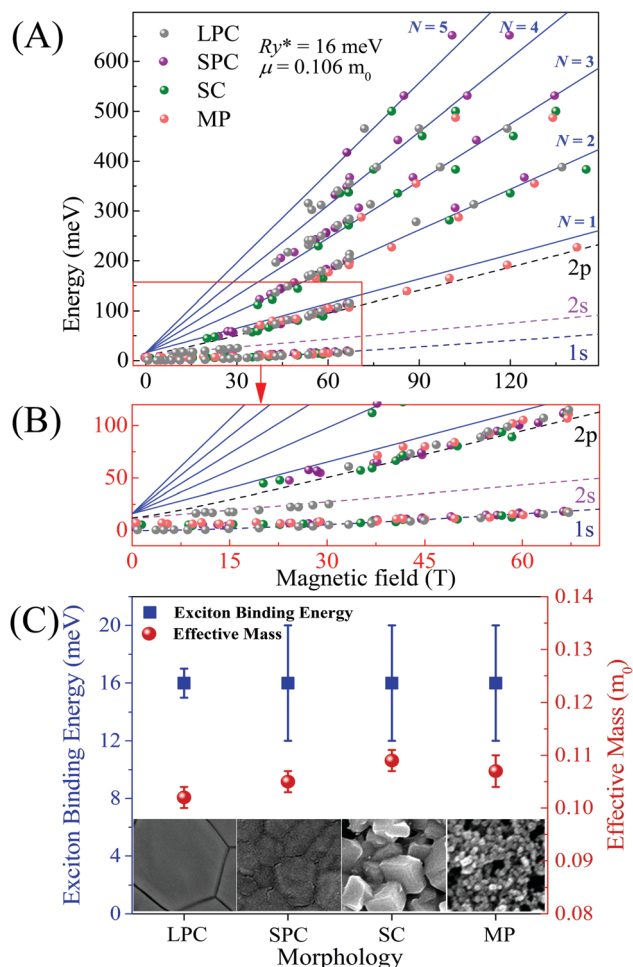


Fig. 3 Comparison of the excitonic properties of the four different MAPbI₃ morphologies. (A) Overlaid fan chart of the LPC, SPC, SC and MP samples. The solid lines and the dashed lines are the fits to the set of Landau levels and the excitonic transitions, respectively. (B) The zoomed-in plot of the excitonic transitions region of the fan chart in panel (A). (C) The bottom panel illustrates the change in Ry* and μ for the various morphologies.

the excitonic characteristics of the corresponding perovskite, Ry* and μ , decreased by less than 15%.¹⁶ The larger steric size of formamidinium compared to methylammonium results in a larger equatorial bond angle (lead–iodide–lead) and, thus, a narrower optical bandgap.⁴⁰ The variation of the crystal size would result in a modified interplay between the organic and the inorganic moieties in the perovskite structure, which in turn changes the strain induced on the crystal structure and thus, impacts the bandgap. The negligible impact that the degree of dipolar cation order and structural arrangement induced by the variation of perovskite microstructure have on the excitonic characteristics might be analogous to the small impact of cation substitution on the excitonic properties, with the lead-halogen sub-unit remaining unchanged in both cases. This indeed demonstrates the critical role of the electronic properties of the inorganic cage in the determination of the excitonic binding energy and reduced effective mass of perovskites. Moreover, this important observation agrees with the recent work

by Perez-Osorio *et al.* in which the largest contribution to the static dielectric constant of MAPbI₃ was demonstrated to originate from the stretching and rocking vibrational modes of the lead–halogen system rather than the internal modes of the organic cation.⁴¹

Using the values obtained for the effective dielectric constant ($\epsilon = \sqrt{Ry^H \times \mu / Ry^* \times m_0}$, where Ry^H = 13.6 eV is the Rydberg constant of the hydrogen atom) and the reduced mass, the Bohr radius of the bound electron–hole system can be calculated. This is similar for all the MAPbI₃ perovskite morphologies and is about 5 nm in the low temperature phase. The Bohr radius is substantially smaller even than the perovskite crystal size of the MP sample and it is consistent with the absence of any signature of a quantum confinement effect on the optical transition of the corresponding excitons in the mesoscopic phase.

The correct interpretation of the optical absorption spectrum for the exciton binding energy derivation in the room temperature tetragonal phase of MAPbI₃ (>160 K) becomes more difficult than in the orthorhombic phase as the large spectral broadening at higher temperatures in the tetragonal phase can potentially mask critical optical transition features even under high magnetic fields.¹⁷ The increased broadening is most likely due to a thermally-induced increase in the orientational disorder and rotational dynamics of the unlocked organic cation above the structural phase transition.⁴² The excitonic binding energy has been reported in the literature^{17,18,24,43} to decrease upon orthorhombic-to-tetragonal phase transition with a likely reason to be the slight increase in the dielectric constant of the medium, which is in turn linked to the increase in the effective phonon energy coupling to the carriers.

We argue that the change in the binding energy at the transition to the tetragonal phase for all the morphologies investigated in this study would be similar. This can be partly understood by the dominant influence of thermal disorder on the electrostatic fluctuations at room temperature over the degree of poly-crystallinity and molecular order which are dominant at lower temperatures;²² the latter properties we have already shown above to have insignificant impact on the electron–hole interaction. This is further supported by a recent theoretical study by Motta *et al.* in which the impact of the degree of molecular dipole orientational disorder – which could be induced by the grain size variation – on the binding energy in the high temperature phase of MAPbI₃ was found to be only ~10%.⁴⁴

To generalise our findings for MAPbI₃ to other perovskite compositions, we repeated the measurements on a state-of-the-art triple-cation lead mixed-halide perovskite, Cs_{0.05}(MA_{0.17}FA_{0.83})_{0.95}Pb(I_{0.83}Br_{0.17})₃.² We consider two significantly different morphologies of this perovskite composition, namely a planar polycrystalline thin film and a film with the perovskite infiltrated into a thick mp-Al₂O₃ scaffold (corresponding SEM images are shown in Fig. S5, ESI†). We show in Fig. S6 (ESI†) that both morphologies exhibit similar magneto-optical responses and, thus, similar fundamental excitonic properties, with the binding energy and reduced mass of 13 ± 2 meV and 0.096 ± 0.008m₀, respectively (see Table S1, ESI†). These results allow us to extend our conclusions to the wider alloyed perovskite family, providing

strong evidence that the microstructure has a negligible impact on the excitonic properties in lead halide perovskites.

Recently, Petrozza and co-workers used temperature-dependent time-resolved transient absorption (TA) spectroscopy to track the fate of excitons following photo-excitation and to understand the relationship between the excitonic properties and film morphology.²² The conclusion from this study was that the exciton binding energy and, therefore, exciton stability can vary depending on the perovskite film microstructure in the tetragonal phase which is most critical to solar cell operation. Their interpretation was based on the emergence and evolution of the negative feature located at the high-energy end of the photobleach signature in the transmission-difference spectrum, which was attributed to self-renormalization of the exciton energy due to a change in its concentration upon decrease in temperature and/or grain size variation. We note that the negative feature developing in the high-energy tail of the TA spectra over time has been proposed to be primarily a consequence of a bandgap renormalization effect (bandgap narrowing) and of a free carrier absorption, among other possible mechanisms.^{45,46} The spectral TA analysis used in ref. 22, which is an indirect technique for characterising excitonic properties, can also be influenced by recombination mechanisms which are strongly influenced by the perovskite crystal morphology. Furthermore, we note from a previous report for MAPbBr₃ perovskite that while Ry* probably remains unchanged by increasing the temperature from 2 K to room temperature, the increase in the broadening of the linear absorption spectra lessens the 1s transition strength.^{18,47} Although this spectral broadening increase is mainly attributed to thermally-activated mechanisms, a change in the intrinsic broadening of perovskites with different microstructures, due for instance to the difference in their inherent structural disorder, can similarly influence the spectral shape while Ry* remains unchanged. This makes unambiguous interpretation of the linear and transient absorption spectra difficult when relying on the detection and the strength of the excitonic feature – at the absorption edge – as these techniques are indirect approaches for Ry* determination compared to the direct approach employed in this study (see Fig. S7 for the zero-field transmission spectra of the four different MAPbI₃ morphologies, ESI†). We note that it is possible there are also transient changes in excitonic populations and properties (*e.g.* due to dynamic photo-excited changes in dielectric constant) that will be averaged out in our steady-state measurements.

Conclusions

We investigated the relationship between the excitonic properties and microstructure of the MAPbI₃ and Cs_{0.05}(MA_{0.17}FA_{0.83})_{0.95}-Pb(I_{0.83}Br_{0.17})₃ perovskites using magneto-optical spectroscopy measurements. We find that the microstructure does not influence the excitonic binding energy of MAPbI₃ or the broader range of mixed-cation and mixed-halide alloyed compositions. This is further supported by recent reports that the same values are also

observed for macroscopic single crystals of MAPbI₃.⁴⁸ Thus, we conclude that excitons truly play a negligible role in the operation of mixed organic–inorganic lead halide-based perovskites regardless of the thin film deposition technique and final morphology, and that excitons need not be a factor for the design of optoelectronic devices based on polycrystalline MAPbI₃ and similar materials with different grain sizes. The universal values of ~16 meV and 0.102–0.109*m*₀ for the exciton binding energy and reduced effective mass in the low-temperature phase of MAPbI₃ can be used as guidelines for interpretation of the spectroscopic data such as the complex spectra of transient absorption measurements. It also implies that the electronic structure of the inorganic cage – (PbI₃)[–] in the case of MAPbI₃ – is likely to have the greatest contribution to the excitonic properties of organic–inorganic lead halide perovskites rather than the degree of poly-crystallinity and the order of dipolar organic cation domains.

Methods

CH₃NH₃PbI₃ (MAPbI₃) Perovskite sample preparation

Large grain polycrystalline film (LPC). LPC perovskite films were prepared using a methylammonium iodide (MAI) and lead acetate Pb(Ac)₂·3H₂O precursor mixture.³² To generate the perovskite solution, MAI (Dyesol) and Pb(Ac)₂·3H₂O were dissolved in anhydrous *N,N*-dimethylformamide at a 3 : 1 molar ratio with final concentration of 30 wt%, and the stabilizer hypophosphorous acid (HPA) was added at a molar ratio of 7.5% with respect to Pb(Ac)₂·3H₂O. Pb(Ac)₂·3H₂O (316512) and HPA (214906) were purchased from Sigma Aldrich. Microscope coverslips were washed sequentially with soap (2 vol% Hellmanex in water), de-ionized water, isopropanol, acetone and finally treated under oxygen plasma for 10 min. The precursor solution was spin-coated at 2000 rpm for 45 s in a nitrogen-filled glovebox, and the substrates were then dried at room temperature for 10 min before annealing at 100 °C for 5 min. The samples were then stored in a nitrogen-filled glovebox until used.

Small grain polycrystalline film (SPC). Soda-lime glass substrates 1 mm thick were purchased from J. Melvin Freed. The substrates were cleaned ultrasonically using soap solution (Hellmanex), water, ethanol and iso-propanol for 15 minutes, each.

PbI₂ (99.99%) was purchased from Alfa Aesar and used without further purification. MAI was either synthesised in-house using a common method or else purchased from Dyesol. All the film preparation work was carried out under nitrogen atmosphere.

MAPbI₃ films were prepared by the “gas-assisted” method of Huang *et al.*³¹ A 25 μL 45 wt% MAPbI₃ DMF solution, prepared from PbI₂ and MAI in a molar ratio of 1 : 1, was spread on the substrate, on a spin-coater. An 80 L min^{–1} stream of nitrogen gas was blown over the film during spinning at 6500 rpm, 2 s after the spinning commenced. The films were annealed at 100 °C on a hotplate for 10 min and then cooled to room temperature.

Small crystal sample (SC). Soda-lime glass substrates treatment and precursor solution (PbI₂ and MAI) preparation were similar to that of the small grain polycrystalline film.

MAPbI₃ films were prepared by the 2-step method of D'Innocenzo *et al.*⁶ The clean glass substrates were heated on a hotplate at 70 °C. A PbI₂ solution in DMF (462 mg mL⁻¹) was warmed to 70 °C and then spin-coated at 2000 rpm for 60 s. The PbI₂ films were subsequently annealed at 70 °C for 30 min. MAPbI₃ films with small crystal size were prepared by dipping the PbI₂-coated substrates in a 0.044 M MAI solution in isopropanol at 25 °C for 2 minutes. Samples were finally rinsed in anhydrous IPA to remove unreacted MAI.

Mesoporous Al₂O₃ (MP). Unless otherwise specified, all materials were purchased from either Alfa Aesar or Sigma-Aldrich and used as received. The synthesis of MAI was performed using the same previously reported method.³¹ The Al₂O₃ (Aldrich, 642991) nanoparticle paste used for characterization measurements was formed by suspending ~45 nm particles in a solution of ethanol, terpineol and ethyl cellulose.

Glass substrates were cleaned by sonication in ethanol for 10 min. The mesoporous Al₂O₃ layer was formed by drop coating approximately 30 μL cm⁻² of the nanoparticle solution on the glass substrates, which were then annealed at 500 °C for 30 min. The perovskite precursor solution was formed by mixing stoichiometric amounts of MAI and PbI₂ in a combination of dimethyl sulfoxide (DMSO) and *N*-methyl-2-pyrrolidone (NMP) (7:3 vol) to form a (46 wt%) concentration solution. Approximately 30 μL cm⁻² of the perovskite precursor solution was applied to the surface of the substrate prior to spin-coating. The films were spin-coated using a two-stage process: 1000 rpm for 5 s using an acceleration of 200 rpm s⁻¹, then 6000 rpm for 50 s using an acceleration of 6000 rpm s⁻¹. A nitrogen gas flow was introduced after 20 s of the second spin-coating step and sustained for a further 20 s. The perovskite films were then annealed on a hot-plate at 100 °C for a duration of 10 min.

Mixed-cation mixed-halide Perovskite sample preparation

The organic cations were purchased from Dyesol; the lead compounds from TCI; Dimethylformamide (DMF), Dimethyl Sulfoxide (DMSO) and cesium iodide from Sigma Aldrich. The mixed cation lead mixed halide perovskite (Cs_{0.05}(MA_{0.17}FA_{0.83})_{0.95}Pb(I_{0.83}Br_{0.17})₃) precursor solutions were prepared by dissolving 1 M FAI, 1.1 M PbI₂, 0.2 M MABr, 0.2 M PbBr₂ in a 4:1 (v:v) mixture of anhydrous DMF:DMSO and 1.5 M stock solution of CsI in DMSO was added to the above solution in a 5:95 (CsI:mixture) volume ratio. The perovskite solutions were then spin coated in a two-step program at 1000 and 6000 rpm for 10 and 30 s respectively. During the second step, 50 μL of chlorobenzene was dripped on the spinning substrate 10 s prior to the end. The perovskite film was annealed at 100 °C for 30 min.

SEM imaging

The LPC samples were imaged using a Zeiss Merlin high-resolution scanning electron microscope with a beam energy of 3 kV. The SPC, SC and MP samples were imaged using a FEI Nova NanoSEM 450 scanning electron microscope unit with a beam energy of 15 kV.

Magneto-optical measurement

The magneto transmission measurements were performed combining long pulse magnetic field measurements and 150 T short duration pulsed magnets.

For the long pulse measurements, the typical duration of the pulse is around 100 ms with the magnetic field up to 66 T. For these measurements, the sample was placed in a liquid helium cryostat. White light from a halogen lamp was used as the excitation source. The light emitted from the lamp was coupled into a 200 μm-diameter multimode fiber, used to illuminate sample. The transmitted light was collected by a 400 μm-diameter multimode fiber and guided to a spectrometer equipped with a liquid nitrogen cooled CCD camera. The typical exposure time was <3 ms, which ensured that the transmission spectra were acquired at an essentially constant magnetic field value.

For very high magnetic field measurements ($B < 150$ T), pulse having a typical duration <10 μs were generated by a single turn coil system with a bore diameter of 10 mm. A non-conducting helium-flow cryostat was located in the single turn coil. The sample was kept at a temperature of ~5 K. Magneto-transmission measurements were conducted using a tunable Optical Parametric Oscillator pumped by a Ti:sapphire laser as the light source. A fast (100 MHz) silicon detector and a high speed digital oscilloscope was used for detection.

Acknowledgements

A. M. S. would like to thank Jincheol Kim for assisting in optimizing the two-step dipping solution-processed samples. The authors acknowledge support from the Australian Government through the Australian Renewable Energy Agency (ARENA) and the Australian Centre for Advanced Photovoltaics (ACAP). The views expressed herein are not necessarily the views of the Australian Government, and the Australian Government does not accept responsibility for any information or advice contained herein. S. D. S. acknowledges funding from the People Programme (Marie Curie Actions) of the European Union's Seventh Framework Programme (FP7/2007-2013) under REA grant agreement number PEOF-GA-2013-622630. This work was partially supported by ANR JCJC project milliPICS, the Région Midi-Pyrénées under contract MESR 13053031, BLAPHENE project under IDEX program Emergence and Programme des Investissements d'Avenir under the program ANR-11-IDEX-0002-02, reference ANR-10-LABX-0037-NEXT. Part of the work has been supported by TERASPEC grant within IDEX Emergence program of University of Toulouse. Zhuo Yang and Nan Zhang hold a fellowship from the Chinese Scholarship Council (CSC). This work was supported by EPSRC (UK) *via* its membership to the EMFL (grant no. EP/N01085X/1). M. A. J. gratefully acknowledges Cambridge Materials Limited for a PhD scholarship.

References

- 1 D. Bi, W. Tress, M. I. Dar, P. Gao, J. Luo, C. Renevier, K. Schenk, A. Abate, F. Giordano, J.-P. Correa Baena, J.-D. Decoppet,

- S. M. Zakeeruddin, M. K. Nazeeruddin, M. Grätzel and A. Hagfeldt, *Sci. Adv.*, 2016, **2**, 1–7.
- 2 M. Saliba, T. Matsui, J.-Y. Seo, K. Domanski, J.-P. Correa-Baena, N. Mohammad, K. S. M. Zakeeruddin, W. Tress, A. Abate, A. Hagfeldt and M. Gratzel, *Energy Environ. Sci.*, 2016, **9**, 1989–1997.
- 3 A. Kojima, K. Teshima, Y. Shirai and T. Miyasaka, *J. Am. Chem. Soc.*, 2009, **131**, 6050–6051.
- 4 N. J. Jeon, J. H. Noh, W. S. Yang, Y. C. Kim, S. Ryu, J. Seo and S. I. Seok, *Nature*, 2015, **517**, 476–480.
- 5 D. P. McMeekin, G. Sadoughi, W. Rehman, G. E. Eperon, M. Saliba, M. T. Hörlantner, A. Haghighirad, N. Sakai, L. Korte, B. Rech, M. B. Johnston, L. M. Herz and H. J. Snaith, *Science*, 2016, **351**, 151–155.
- 6 V. D’Innocenzo, A. R. Srimath Kandada, M. De Bastiani, M. Gandini and A. Petrozza, *J. Am. Chem. Soc.*, 2014, **136**, 17730–17733.
- 7 C. G. Bischak, E. M. Sanehira, J. T. Pecht, J. M. Luther and N. S. Ginsberg, *Nano Lett.*, 2015, **15**, 4799–4807.
- 8 Z.-K. Tan, R. S. Moghaddam, M. L. Lai, P. Docampo, R. Higler, F. Deschler, M. Price, A. Sadhanala, L. M. Pazos, D. Credgington, F. Hanusch, T. Bein, H. J. Snaith and R. H. Friend, *Nat. Nanotechnol.*, 2014, **9**, 687–692.
- 9 M. Saliba, S. M. Wood, J. B. Patel, P. K. Nayak, J. Huang, J. A. Alexander-Webber, B. Wenger, S. D. Stranks, M. T. Hörlantner, J. T.-W. Wang, R. J. Nicholas, L. M. Herz, M. B. Johnston, S. M. Morris, H. J. Snaith and M. K. Riede, *Adv. Mater.*, 2016, **28**, 923–929.
- 10 M. A. Green, A. Ho-Baillie and H. J. Snaith, *Nat. Photonics*, 2014, **8**, 506–514.
- 11 S. D. Stranks and H. J. Snaith, *Nat. Nanotechnol.*, 2015, **10**, 391–402.
- 12 T. Ishihara, *J. Lumin.*, 1994, **60-61**, 269–274.
- 13 M. Hirasawa, T. Ishihara, T. Goto, K. Uchida and N. Miura, *Phys. B*, 1994, **201**, 427–430.
- 14 M. Hirasawa, T. Ishihara and T. Goto, *J. Phys. Soc. Jpn.*, 1994, **63**, 3870–3879.
- 15 M. E. Ziffer, J. C. Mohammed and D. S. Ginger, *ACS Photonics*, 2016, **3**, 1060–1068.
- 16 K. Galkowski, A. Mitioglu, a. miyata, p. plochocka, o. Portugall, G. E. Eperon, J. T.-W. Wang, T. Stergiopoulos, S. D. Stranks, H. Snaith and R. J. Nicholas, *Energy Environ. Sci.*, 2016, **9**, 962–970.
- 17 A. Miyata, A. Mitioglu, P. Plochocka, O. Portugall, J. T.-W. Wang, S. D. Stranks, H. J. Snaith and R. J. Nicholas, *Nat. Phys.*, 2015, **11**, 582–587.
- 18 A. M. Soufiani, F. Huang, P. Reece, R. Sheng, A. Ho-Baillie and M. A. Green, *Appl. Phys. Lett.*, 2015, **107**, 231902.
- 19 Y. Fu, H. Zhu, C. C. Stoumpos, Q. Ding, J. Wang, M. G. Kanatzidis, X. Zhu and S. Jin, *ACS Nano*, 2016, **10**, 7963–7972.
- 20 S. A. March, D. B. Riley, C. Clegg, D. Webber, X. Liu, M. Dobrowolska, J. K. Furdyna, I. G. Hill and K. C. Hall, *arXiv preprint arXiv:1602.05186*, 2016.
- 21 A. R. Srimath Kandada and A. Petrozza, *Acc. Chem. Res.*, 2016, **49**, 536–544.
- 22 G. Grancini, A. R. Srimath Kandada, J. M. Frost, A. J. Barker, M. De Bastiani, M. Gandini, S. Marras, G. Lanzani, A. Walsh and A. Petrozza, *Nat. Photonics*, 2015, **9**, 695–701.
- 23 Q. Lin, A. Armin, R. C. R. Nagiri, P. L. Burn and P. Meredith, *Nat. Photonics*, 2014, **9**, 106–112.
- 24 J. Even, L. Pedesseau and C. Katan, *J. Phys. Chem. C*, 2014, **118**, 11566–11572.
- 25 V. D’Innocenzo, G. Grancini, M. J. P. Alcocer, A. R. S. Kandada, S. D. Stranks, M. M. Lee, G. Lanzani, H. J. Snaith and A. Petrozza, *Nat. Commun.*, 2014, **5**, 3586.
- 26 L. M. Herz, *Annu. Rev. Phys. Chem.*, 2016, **67**, 65–89.
- 27 J. Kim, J. S. Yun, X. Wen, A. M. Soufiani, C. F. J. Lau, B. Wilkinson, J. Seidel, M. A. Green, S. Huang and A. W. Y. Ho-Baillie, *J. Phys. Chem. C*, 2016, **120**, 11262–11267.
- 28 J. Burschka, N. Pellet, S.-J. Moon, R. Humphry-Baker, P. Gao, M. K. Nazeeruddin and M. Gratzel, *Nature*, 2013, **499**, 316–319.
- 29 W. S. Yang, J. H. Noh, N. J. Jeon, Y. C. Kim, S. Ryu, J. Seo and S. I. Seok, *Science*, 2015, **348**, 1234–1237.
- 30 M. Liu, M. B. Johnston and H. J. Snaith, *Nature*, 2013, **501**, 395–398.
- 31 F. Huang, Y. Dkhissi, W. Huang, M. Xiao, I. Benesperi, S. Rubanov, Y. Zhu, X. Lin, L. Jiang and Y. Zhou, *Nano Energy*, 2014, **10**, 10–18.
- 32 W. Zhang, S. Pathak, N. Sakai, T. Stergiopoulos, P. K. Nayak, N. K. Noel, A. A. Haghighirad, V. M. Burlakov, D. W. deQuilettes, A. Sadhanala, W. Li, L. Wang, D. S. Ginger, R. H. Friend and H. J. Snaith, *Nat. Commun.*, 2015, **6**, 10030.
- 33 C. F. Klingshirn, *Semiconductor optics*, Springer, 2007.
- 34 J. Tilchin, D. N. Dirin, G. I. Maikov, A. Sashchiuk, M. V. Kovalenko and E. Lifshitz, *ACS Nano*, 2016, **10**, 6363–6371.
- 35 P. C. Makado and N. C. McGill, *J. Phys. C: Solid State Phys.*, 1986, **19**, 873.
- 36 G. Mahan, *Proc. 1971 Antwerp Advanced Study Inst*, 1972.
- 37 D. Li, G. Wang, H.-C. Cheng, C.-Y. Chen, H. Wu, Y. Liu, Y. Huang and X. Duan, *Nat. Commun.*, 2016, **7**, 11330.
- 38 A. Osherov, E. M. Hutter, K. Galkowski, R. Brenes, D. K. Maude, R. J. Nicholas, P. Plochocka, V. Bulović, T. J. Savenije and S. D. Stranks, *Adv. Mater.*, 2016, **28**, 10757–10763.
- 39 K. Galkowski, A. A. Mitioglu, A. Surrente, Z. Yang, D. K. Maude, P. Kossacki, G. E. Eperon, J. T. W. Wang, H. J. Snaith, P. Plochocka and R. J. Nicholas, *Nanoscale*, 2017, **9**, 3222.
- 40 M. R. Filip, G. E. Eperon, H. J. Snaith and F. Giustino, *Nat. Commun.*, 2014, **5**, 5757.
- 41 M. A. Pérez-Osorio, R. L. Milot, M. R. Filip, J. B. Patel, L. M. Herz, M. B. Johnston and F. Giustino, *J. Phys. Chem. C*, 2015, **119**, 25703–25718.
- 42 A. M. A. Leguy, A. R. Goni, J. M. Frost, J. Skelton, F. Brivio, X. Rodriguez-Martinez, O. J. Weber, A. Pallipurath, M. I. Alonso, M. Campoy-Quiles, M. T. Weller, J. Nelson, A. Walsh and P. R. F. Barnes, *Phys. Chem. Chem. Phys.*, 2016, **18**, 27051–27066.
- 43 Y. Yamada, T. Nakamura, M. Endo, A. Wakamiya and Y. Kanemitsu, *IEEE J. Photovolt.*, 2014, 401–405.
- 44 C. Motta, P. Mandal and S. Sanvito, *Phys. Rev. B: Condens. Matter Mater. Phys.*, 2016, **94**, 045202.

- 45 M. B. Price, J. Butkus, T. C. Jellicoe, A. Sadhanala, A. Briane, J. E. Halpert, K. Broch, J. M. Hodgkiss, R. H. Friend and F. Deschler, *Nat. Commun.*, 2015, **6**, 8420.
- 46 Y. Yang, D. P. Ostrowski, R. M. France, K. Zhu, J. van de Lagemaat, J. M. Luther and M. C. Beard, *Nat. Photonics*, 2015, **10**, 53–59.
- 47 N. Sestu, M. Cadelano, V. Sarritzu, F. Chen, D. Marongiu, R. Piras, M. Mainas, F. Quochi, M. Saba, A. Mura and G. Bongiovanni, *J. Phys. Lett.*, 2015, **6**, 4566–4572.
- 48 Z. Yang, A. Surrente, K. Galkowski, N. Bruyant, D. K. Maude, A. A. Haghighirad, H. J. Snaith, P. Plochocka and R. J. Nicholas, *J. Phys. Chem. Lett.*, 2017, **8**, 1851–1855.